Mechanics of Materials 160 (2021) 103998

Contents lists available at ScienceDirect

Mechanics of Materials

journal homepage: www.elsevier.com/locate/mechmat

# Phase evolution based thermomechanical crack closure mechanism of shape memory polymers

A. Foyouzat [a], H. Bayesteh [a,b], S. Mohammadi [a,*]

[a] High Performance Computing Lab, School of Civil Engineering, Faculty of Engineering, University of Tehran, Tehran, Iran
[b] Faculty of Civil, Water & Environmental Engineering, Shahid Beheshti University, Tehran, Iran

ARTICLE INFO

*Keywords:*
Shape memory polymer (SMP)
Fracture analysis
Smart materials
eXtended finite element method (XFEM)
Self-healing

ABSTRACT

In this article, the thermomechanical fracture responses of shape memory polymers (SMPs) under two common *stress free- strain recovery* and *fixed strain- stress recovery* loading cycles are investigated. The shape memory properties of cracked SMPs for both single and mixed fracture modes are examined. The effect of phase transformation on the fracture parameters of the material is evaluated by the extended finite element method (XFEM). In addition, the fracture behavior is studied when the crack is created during the thermomechanical process. The results show that the initially cracked SMPs can fully preserve the shape memory property for both *stress free-strain recovery* and *fixed strain- stress recovery* cycles. Moreover, as a promising application, SMPs can be well employed in self-healing materials due to complete closure of the crack at the end of the shape recovery cycle. In cases where a crack is created in the midst of the *fixed strain- stress recovery* thermomechanical process, it is observed that the performance of the structure in providing desired reaction forces is reduced by increase of the crack length. Nevertheless, the presence of compressive forces in the initial steps of the force recovery cycle may potentially contribute to crack healing if additive healing agents are employed.

## 1. Introduction

In recent decades, there is a growing interest in the study of shape memory polymers (SMPs), as a class of smart materials, capable of switching between temporary and original shapes due to external stimuli. In comparison to other smart materials, such as shape memory alloys and shape memory ceramics, SMPs enjoy the economic advantage, lighter weight and easier manufacturing process (Leng et al., 2011). Moreover, thanks to the advantage of being a biocompatible and biodegradable capability, they have received much attention in the last two decades (Leng et al., 2009). For example, SMPs have been utilized in many engineering applications such as actuators (Chen et al., 2019; Baniasadi et al., 2020), sensor devices (Leo et al., 2018) and deployable hinges in the aerospace industry (Liu et al., 2014), or serve as stents in cardiovascular systems for biomedical applications (Govindarajan and Shandas, 2014).

Despite various external stimuli methods, including thermal (Diani et al., 2012), electrical (Liu et al., 2009), PH (Han et al., 2012), and light-induced activation (Lendlein et al., 2005), thermal stimulation is the most common mechanism in SMP activation. In this case, the intrinsic property which activates the material is a particular temperature, called the glass transition temperature ($T_g$). Below $T_g$, the material is mainly in the "glassy phase" where it behaves in a brittle manner. At temperatures higher than $T_g$, the secondary phase, called the "rubbery phase", dominates the material with much deformable and softer behavior than that in the glassy state (Leng et al., 2011).

Fig. 1 schematically illustrates the most important property of SMP, namely the shape memory effect (SME) in a temperature-stress-strain diagram. The thermomechanical loading cycle starts at point ① where the material is in a free stress-strain situation (point ① is the state that defines the permanent shape of the material). At this state, the SMP undergoes a pure mechanical loading at a high temperature ($T_h > T_g$) until it reaches to point ②. At this loading step, the material is essentially in the rubbery phase, where it behaves in a ductile manner. At state ②, the deformation is held fixed while the temperature is decreased to a low temperature ($T_l < T_g$) until the currently rubbery SMP gradually transforms into the glassy brittle material (point ③). Thereafter, by removing the external mechanical loading, the material experiences a rather small deformation (point ④) which is due to the high stiffness of SMP in the glassy phase in comparison with the rubbery phase. At this point, the material holds its current temporary shape. In

* Corresponding author.
*E-mail address:* smoham@ut.ac.ir (S. Mohammadi).

https://doi.org/10.1016/j.mechmat.2021.103998
Received 3 December 2020; Received in revised form 4 June 2021; Accepted 15 July 2021
Available online 20 July 2021

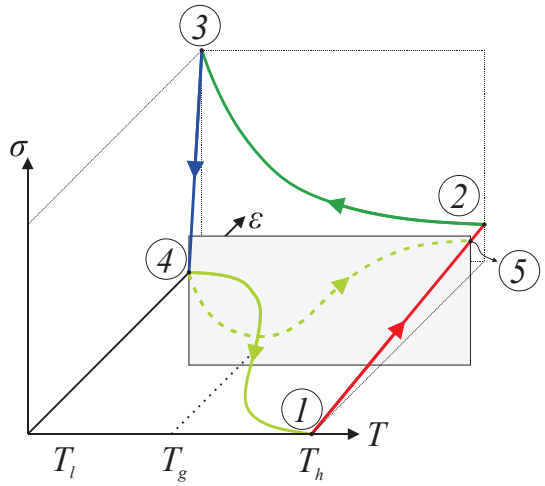


**Fig. 1.** Schematic presentation of thermomechanical cycles of shape memory polymers, including stress free- strain recovery (①-②-③-④-①) and fixed strain- stress recovery (①-②-③-④-⑤).

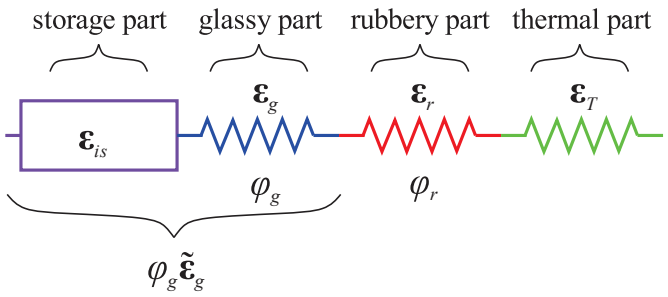


**Fig. 2.** Schematic representation of the constitutive model proposed by Baghani et al. (Baghani et al., 2012a).

the final thermomechanical loading step, the ambient temperature is increased ($T_h > T_g$) without applying any external mechanical loading. As a result, as the SMP transforms from the glassy phase to the rubbery phase, the material recovers its original shape, i.e., point ①. This thermomechanical cycle is called the *stress free-strain recovery* cycle in SMPs. It should be noted that at point ④, if the temperature is increased while the deformation is held fixed, the material would reach to state ⑤, and the recovery process is called the *fixed strain-stress recovery*.

Despite remarkable properties of SMPs, these materials are highly prone to damage and fracture when subjected to thermomechanical loading due to their low strength and poor elastic properties (Nji and Li, 2012; Abbasi-Shirsavar et al., 2019; Foyouzat et al., 2020). While various numerical and experimental studies can be found in the literature on the study of fracture behavior of different smart materials (such as shape memory alloys (SMAs) (Wang et al., 2010; Maletta et al., 2014; Baxevanis et al., 2013; HatefiArdakani et al., 2016, 2019; FatemiDehaghani et al., 2017) and shape memory ceramics (SMCs) (Tavangarian and Li, 2015; Moshkelgosha and Mamivand, 2020; Du et al., 2015), few researches have been carried out on SMPs. Therefore, further study is required in order to investigate the fracture behavior of SMPs and to examine their shape memory effects in self-healing applications.

The overall healing process in polymers involves two main steps: Close Then Heal (CTH), where first the two crack faces overlap together (Close) and then heal the defect using the healing agents (like microcapsules, …) (Li and Uppu, 2010). For instance, Plaisted and Nemat-Nasser (2007) examined the self- healing potential of 2 MEP4F polymer under repeated fracture and healing cycles using the double cleavage drilled compression (DCDC) specimens. They found that the toughness of the healed specimen nearly doubled over several fracture-healing cyclic loadings (Plaisted and Nemat-Nasser, 2007). Malakooti et al. (Kazemi-Lari et al., 2017) proposed a self- healing mechanism for a shape memory polyurethane by heating the polymer using an embedded optical fiber. In another research, Zhang et al. (2018) proposed a self-healable composite, made of synthetic foam as matrix, a honeycomb structure as reinforcement and a healing agent. Moreover, Karimi et al. (2019) used SMA fibers as healing agents of SMA composites and evaluated the effect of fiber volume fraction in healing cracks.

The present study is devoted to the thermomechanical fracture analysis of shape memory polymers under various thermomechanical loading conditions and their potential capability in crack closure mechanism. First, the phase transition based constitutive model for SMP material is presented. Then, the governing equations including the finite element discretization are discussed. In the next section, the thermomechanical XFEM formulation and the corresponding governing equations are presented. Finally, the paper deals with a number of simulations of stationary crack in SMP problems in order to investigate the shape memory property of a cracked SMP and the corresponding closure mechanisms. Where possible, the results are validated by available experimental observations.

## 2. Constitutive model of SMP

There are several phenomenological constitutive models available in literature for shape memory polymers. These models mainly discuss the macroscopic continuum nature of materials without going into the details of underlying microscopic structure. In general, two types of constitutive models are used to characterize the behavior of SMPs, namely, viscoelastic models (Tobushi et al., 1997; Diani et al., 2006; Zeng et al., 2018; Gu et al., 2019) and phase transition models (Zhao et al., 2020; Liu et al., 2006; Chen and Lagoudas, 2008a, 2008b; Baghani et al., 2012a; Boatti et al., 2016).

In models based on viscoelasticity, originally developed by Tobushi et al. (1997), the behavior of SMP is explained using the combinations of simple springs, dashpots, and frictional elements. In the phase transition models, the frozen and active phases of SMP are accounted for based on the molecular mechanism and experimental observations (Leng et al., 2011). For example, Liu et al. (2006) initially proposed a 1D phase transition constitutive model for amorphous SMPs in the small strain states.

Then, Chen and Lagoudas, 2008a, 2008b further developed the model of Liu et al. (2006) to 3D small (Chen and Lagoudas, 2008b) and large deformation (Chen and Lagoudas, 2008a) regimes and illustrated that the linearized small-strain model can well perform for up to 10% applied strain on epoxy SMP of the experiments by Liu et al. (2006).

Moreover, Volk et al., 2010a, 2010b performed experiments on Veriflex SMP and employed the model of Chen and Lagoudas, 2008a, 2008b to calibrate the material parameters. Later, Baghani et al. (2012a) improved the model of Liu et al. (2006) by introducing a new evolution law in the heating process to propose a small-strain constitutive model. They studied the behavior of SMP prismatic bars under torsion and validated their results with the experiments performed by Diani et al. (2011). Although their proposed model was based on a small strain formulation, they reported successful prediction of the experimental material response of up to moderate strains, as large as 8%. Further information on SMP constitutive models can be found in (Yarali et al., 2020).

In this study, an improved phase transition-based constitutive model, proposed by Baghani et al. (2012a), is adopted, which is based on the original model of Liu et al. (2006). According to this model and the rule of mixture in a small strain regime, the total strain can be expressed as (see Fig. 2 (Baghani et al., 2012a))

$$\boldsymbol{\varepsilon} = \phi_r \boldsymbol{\varepsilon}_r + \phi_g \tilde{\boldsymbol{\varepsilon}}_g + \boldsymbol{\varepsilon}_T \tag{1}$$

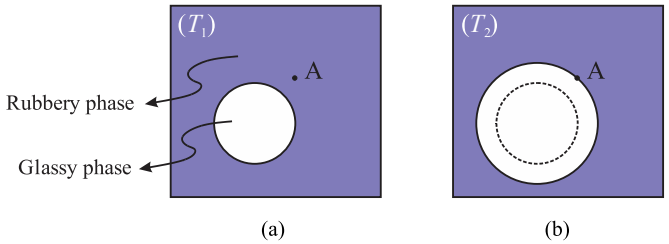


**Fig. 3.** Strain storage process at point A; the glassy zone evolves by decreasing the temperature ($T_2<T_1$).

where $\boldsymbol{\varepsilon}_r$ and $\widetilde{\boldsymbol{\varepsilon}}_g$ represent the elastic strains in the rubbery and glassy phases, respectively, while $\boldsymbol{\varepsilon}_T$ describes the thermal strain defined as:

$$\boldsymbol{\varepsilon}_T = \int \alpha_{eff}(T)\ dT \tag{2}$$

in which $\alpha_{eff}$ is the effective coefficient of thermal expansion of the material. In addition, $\phi_r$ and $\phi_g$ are temperature dependent volume fractions of the rubbery and glassy phases, respectively, with the constraint of:

$$\phi_r + \phi_g = 1 \tag{3}$$

### 2.1. Inelastic strain storage and strain recovery mechanisms

The strain storage and strain recovery processes occur in paths ②-③ and ④-① in the *stress free-strain recovery* (or ④-⑤ in the *fixed strain-stress recovery*) cycle, respectively, as shown in Fig. 1. In the strain storage process, a new glassy phase zone, previously in the rubbery phase, is created by reducing the temperature (for example, point A in Fig. 3). Since this zone has experienced the strain $\boldsymbol{\varepsilon}_r$ before the transition to the glassy phase, one may write (Baghani et al., 2012a):

$$\phi_g\widetilde{\boldsymbol{\varepsilon}}_g = \phi_g\left(\boldsymbol{\varepsilon}_g + \overline{\boldsymbol{\varepsilon}}_g\right) = \phi_g\left(\boldsymbol{\varepsilon}_g + \frac{1}{V_g}\int_{V_g}\boldsymbol{\varepsilon}_r\ dv\right) = \phi_g\boldsymbol{\varepsilon}_g + \frac{1}{V_0}\int_{V_g}\boldsymbol{\varepsilon}_r\ dv \tag{4}$$

where $V_g$ and $V_0$ denote the volume of the glassy phase and the total volume of SMP, respectively. Therefore, Eq. (4) can be rewritten as:

$$\phi_g\widetilde{\boldsymbol{\varepsilon}}_g = \phi_g\boldsymbol{\varepsilon}_g + \int \boldsymbol{\varepsilon}_r\ d\phi_g = \phi_g\boldsymbol{\varepsilon}_g + \boldsymbol{\varepsilon}_{is} \tag{5}$$

where $\boldsymbol{\varepsilon}_{is}$ refers to the so-called "inelastic stored strain", as introduced by Liu et al. (2004). Therefore, in the cooling process, the inelastic stored strain becomes:

$$\boldsymbol{\varepsilon}_{is} = \int \boldsymbol{\varepsilon}_r\ d\phi_g \tag{6}$$

In the recovery process, which takes place through the heating of material, the inelastic strain stored in step ②-③ is released. This process can be mathematically described as:

$$\phi_g\widetilde{\boldsymbol{\varepsilon}}_g = \phi_g\left(\boldsymbol{\varepsilon}_g + \frac{1}{V_g}\int_{V_g}\frac{\boldsymbol{\varepsilon}_{is}}{\phi_g}\ dv\right) = \phi_g\boldsymbol{\varepsilon}_g + \frac{1}{V_0}\int_{V_g}\frac{\boldsymbol{\varepsilon}_{is}}{\phi_g}\ dv \tag{7}$$

or equivalently

$$\phi_g\widetilde{\boldsymbol{\varepsilon}}_g = \phi_g\boldsymbol{\varepsilon}_g + \int_{V_g}\frac{\boldsymbol{\varepsilon}_{is}}{\phi_g}\ d\phi_g = \phi_g\boldsymbol{\varepsilon}_g + \boldsymbol{\varepsilon}_{is} \tag{8}$$

As a result, the stored strain in the heating process may be written as:

$$\boldsymbol{\varepsilon}_{is} = \int_{V_g}\frac{\boldsymbol{\varepsilon}_{is}}{\phi_g}\ d\phi_g \tag{9}$$

Examining Eqs. (6) and (9), it can be concluded that the stored strain is only a function of the temperature rate. These two equations suggest that the evolution law for the stored strain has the following form:

$$\dot{\boldsymbol{\varepsilon}}_{is} = \kappa_1\int \boldsymbol{\varepsilon}_r\ d\varphi_g + \kappa_2\int\frac{\boldsymbol{\varepsilon}_{is}}{\varphi_g}\ d\varphi_g; \quad \begin{cases} \kappa_1 = 1, & \kappa_2 = 0; & \dot{T} < 0 \\ \kappa_1 = 0, & \kappa_2 = 1; & \dot{T} > 0 \\ \kappa_1 = 0, & \kappa_2 = 0; & \dot{T} = 0 \end{cases} \tag{10}$$

where $\dot{()} = \partial/\partial t$ stands for the derivative with respect to time and the coefficients $\kappa_i$ (i = 1,2) are used to determine whether the temperature is increasing or decreasing.

### 2.2. Helmholtz free energy function

According to the mixture rule, the convex Helmholtz's free energy function ($\overline{\Psi}$) for a shape memory polymer may be expressed in the form of (for more details see reference (Baghani et al., 2012a)):

$$\begin{aligned}\overline{\Psi}\left(\phi_r,\phi_g,\boldsymbol{\varepsilon},\boldsymbol{\varepsilon}_r,\boldsymbol{\varepsilon}_g,\boldsymbol{\varepsilon}_{is},T\right) &= \phi_r\overline{\Psi}_r(\boldsymbol{\varepsilon}_r) + \phi_g\overline{\Psi}_g\left(\boldsymbol{\varepsilon}_g\right) \\ &+ \overline{\Psi}_\lambda\left(\phi_r,\phi_g,\boldsymbol{\varepsilon},\boldsymbol{\varepsilon}_r,\boldsymbol{\varepsilon}_g,\boldsymbol{\varepsilon}_{is},T\right) + \overline{\Psi}_T(T)\end{aligned} \tag{11}$$

where $\overline{\Psi}_r$ and $\overline{\Psi}_g$ are the Helmholtz free energy functions for rubbery and glassy phases, respectively, $\overline{\Psi}_T$ is the thermal energy, and $\overline{\Psi}_\lambda$ is the free energy function due to the kinematic constraints of Eq. (1). In order to impose the constraint of Eq. (1), the Lagrange multiplier technique may be adopted:

$$\overline{\Psi}_\lambda\left(\phi_r,\phi_g,\boldsymbol{\varepsilon},\boldsymbol{\varepsilon}_r,\boldsymbol{\varepsilon}_g,\boldsymbol{\varepsilon}_{is},T\right) = \boldsymbol{\lambda} : \left[\boldsymbol{\varepsilon} - \left(\phi_r\boldsymbol{\varepsilon}_r + \phi_g\boldsymbol{\varepsilon}_g + \boldsymbol{\varepsilon}_{is}\right) - \boldsymbol{\varepsilon}_T\right] \tag{12}$$

where $\boldsymbol{\lambda}$ is the Lagrange multiplier tensor.

### 2.3. Thermodynamics constraint

To extract the necessary constraints on the evolution equations, the Clasius-Duhem inequality statement of the second law of thermodynamics is adopted:

$$\boldsymbol{\sigma} : \dot{\boldsymbol{\varepsilon}} - (\dot{\overline{\Psi}} + \eta\,\dot{T}) \geq 0 \tag{13}$$

where $\eta$ is the entropy. Substituting $\Psi$ from Eq. (11) into inequality (13) results in (Baghani et al., 2012a):

$$\begin{aligned}&\boldsymbol{\sigma} : \dot{\boldsymbol{\varepsilon}} - \phi_r\frac{\partial\overline{\Psi}_r(\varepsilon_r)}{\partial\varepsilon_r} : \dot{\boldsymbol{\varepsilon}}_r - \phi_g\frac{\partial\overline{\Psi}_g(\varepsilon_g)}{\partial\varepsilon_g} : \dot{\boldsymbol{\varepsilon}}_g - \frac{\partial\overline{\Psi}}{\partial\phi_g}\phi_g'\dot{T} - \Psi_T'\,\dot{T} \\ &\quad - \left[\boldsymbol{\varepsilon} - \left(\phi_r\boldsymbol{\varepsilon}_r + \phi_g\boldsymbol{\varepsilon}_g + \boldsymbol{\varepsilon}_{is}\right) - \boldsymbol{\varepsilon}_T\right] : \dot{\boldsymbol{\lambda}} \\ &- \left[\dot{\boldsymbol{\varepsilon}} - \left(\phi_r\dot{\boldsymbol{\varepsilon}}_r + \phi_g\dot{\boldsymbol{\varepsilon}}_g + \phi_g'(\boldsymbol{\varepsilon}_g - \boldsymbol{\varepsilon}_r)\dot{T} + \dot{\boldsymbol{\varepsilon}}_{is}\right) - \boldsymbol{\varepsilon}_T'\dot{T}\right] : \boldsymbol{\lambda} - \eta\,\dot{T} \geq 0\end{aligned} \tag{14}$$

where $()' = \partial/\partial T$ represents the derivative with respect to temperature. Noting that the inequality (14) needs to hold for an arbitrary choice of variables $\dot{\boldsymbol{\varepsilon}}$, $\dot{\boldsymbol{\varepsilon}}_r$, $\dot{\boldsymbol{\varepsilon}}_g$, $\dot{T}$ and $\dot{\boldsymbol{\lambda}}$, it follows that (Baghani et al., 2012a):

$$\boldsymbol{\sigma} = \boldsymbol{\lambda} = \frac{\partial\overline{\Psi}_r(\boldsymbol{\varepsilon}_r)}{\partial\boldsymbol{\varepsilon}_r} = \frac{\partial\overline{\Psi}_g(\boldsymbol{\varepsilon}_g)}{\partial\boldsymbol{\varepsilon}_g} \tag{15}$$

$$\boldsymbol{\varepsilon} = \phi_r\boldsymbol{\varepsilon}_r + \phi_g\boldsymbol{\varepsilon}_g + \boldsymbol{\varepsilon}_{is} + \boldsymbol{\varepsilon}_T \tag{16}$$

$$\eta = -\Psi_T' + \boldsymbol{\sigma} : \left(\boldsymbol{\varepsilon}_T' + \phi_g'\left(\boldsymbol{\varepsilon}_g + (\kappa_1 - 1)\boldsymbol{\varepsilon}_r + \kappa_2\frac{\boldsymbol{\varepsilon}_{is}}{\phi_g}\right)\right) - \frac{\partial\overline{\Psi}}{\partial\phi_g}\phi_g' \tag{17}$$

Eqs. (15)-(17) are the result of a number of fundamental assumptions such as: simultaneous existence of rubbery and glassy phases, strain decomposition, definition of the Helmholtz free energy function, evolution equations and satisfaction of the second law of thermodynamics. The following quadratic forms are used for the Helmholtz free energy function in the small strain regime (Baghani et al., 2012a):

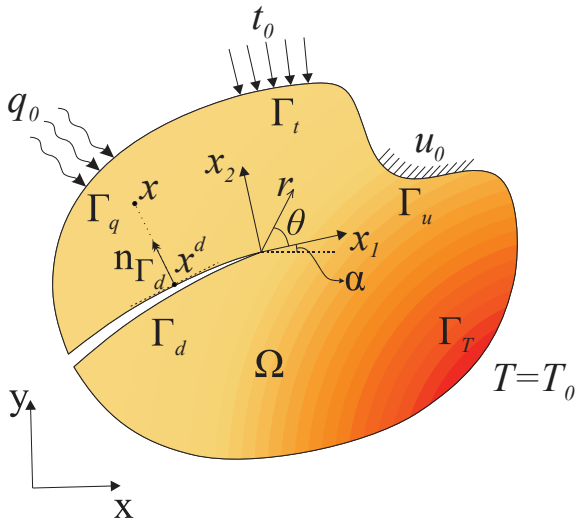


**Fig. 4.** *Thermomechanical loading and boundary conditions of a shape memory polymer.*

$$\overline{\Psi}_r(\boldsymbol{\varepsilon}_r)=\frac{1}{2}\boldsymbol{\varepsilon}_r:\mathbb{C}_r:\boldsymbol{\varepsilon}_r \quad \overline{\Psi}_g(\boldsymbol{\varepsilon}_g)=\frac{1}{2}\boldsymbol{\varepsilon}_g:\mathbb{C}_g:\boldsymbol{\varepsilon}_g \tag{18}$$

where $\mathbb{C}_r$ and $\mathbb{C}_g$ are the fourth order tensors of rubbery and glassy phases, respectively, which in the matrix form can be written as

$$\mathbf{C}_i=\begin{cases}\dfrac{E_i}{1-\nu_i^2}\begin{Bmatrix}1 & \nu_i & 0\\ \nu_i & 1 & 0\\ 0 & 0 & (1-\nu_i)/2\end{Bmatrix} & plane\ \ stress\\ \dfrac{E_i}{(1+\nu_i)(1-2\nu_i)}\begin{Bmatrix}1-\nu_i & \nu_i & 0\\ \nu_i & 1-\nu_i & 0\\ 0 & 0 & 0.5-\nu_i\end{Bmatrix} & Plane\ \ strain\end{cases} \tag{19}$$

which $i=r,g$ states the phase of material in each of the rubbery and glassy phases and $E,\nu$ represent the elasticity modulus and the Poisson's ratio of the material, respectively.

### 2.4. Discrete form of the constitutive model

In this section, the consistent tangent matrix of the proposed model is presented. Assuming the goal is to perform the analysis at step $n+1$, using Eq. (15)

$$\boldsymbol{\sigma}^{n+1}=\mathbf{C}_i\boldsymbol{\varepsilon}_i^{n+1} \quad (i=r,g) \tag{20}$$

Writing the strain $\boldsymbol{\varepsilon}_g$ in terms of $\boldsymbol{\varepsilon}_r$ results in

$$\boldsymbol{\varepsilon}_g^{n+1}=\mathbf{C}_g^{-1}\left(\mathbf{C}_r\boldsymbol{\varepsilon}_r^{n+1}\right) \tag{21}$$

Substituting (21) into (16), the total strain may be written as

$$\boldsymbol{\varepsilon}^{n+1}=\varphi_g\left(T^{n+1}\right)\mathbf{C}_g^{-1}\left(\mathbf{C}_r\boldsymbol{\varepsilon}_r^{n+1}\right)+\varphi_r\left(T^{n+1}\right)\boldsymbol{\varepsilon}_r^{n+1}+\boldsymbol{\varepsilon}_{is}^{n+1}+\boldsymbol{\varepsilon}_T^{n+1} \tag{22}$$

Moreover, the time discretization of the inelastic strain evolution Eq. (10) is (Baghani et al., 2012b)

$$\begin{aligned}\boldsymbol{\varepsilon}_{is}^{n+1}&=\left[1-\left(\varphi_g\left(T^{n+1}\right)-\varphi_g\left(T^n\right)\right)\frac{\kappa_2}{\varphi_g\left(T_{n+1}\right)}\right]^{-1}\left(\boldsymbol{\varepsilon}_{is}^n\left(\varphi_g\left(T^{n+1}\right)-\varphi_g\left(T^n\right)\right)\kappa_1\boldsymbol{\varepsilon}_r\right)\\&=\Lambda\left(\boldsymbol{\varepsilon}_{is}^n+\left(\varphi_g\left(T^{n+1}\right)-\varphi_g\left(T^n\right)\right)\kappa_1\boldsymbol{\varepsilon}_r\right)\end{aligned} \tag{23}$$

Substituting (23) into (22) and solving Eq. (22) for $\boldsymbol{\varepsilon}_r^{n+1}$ yields to

$$\boldsymbol{\varepsilon}_r^{n+1}=\mathbf{H}^{-1}.\boldsymbol{e} \tag{24}$$

where

$$\begin{aligned}\mathbf{H}&=\varphi_g\left(T^{n+1}\right)\mathbf{C}_g^{-1}\mathbf{C}_r\\&+\left(\left(1-\varphi_g\left(T^{n+1}\right)\right)+\kappa_1\Lambda\left(\varphi_g\left(T^{n+1}\right)-\varphi_g\left(T^n\right)\right)\right)\mathbf{I}\end{aligned} \tag{25}$$

$$\boldsymbol{e}=\boldsymbol{\varepsilon}^{n+1}-\Lambda\boldsymbol{\varepsilon}_{is}^n-\boldsymbol{\varepsilon}_T^{n+1} \tag{26}$$

Then, Eq. (20), is transformed to

$$\begin{aligned}\boldsymbol{\sigma}^{n+1}&=\mathbf{C}_r\boldsymbol{\varepsilon}_r^{n+1}=\mathbf{C}_r.\mathbf{H}^{-1}.\boldsymbol{e}\\&=\mathbf{C}_r.\left\{\varphi_g\left(T^{n+1}\right)\mathbf{C}_g^{-1}\mathbf{C}_r+\left(\left(1-\varphi_g\left(T^{n+1}\right)\right)+\kappa_1\Lambda\left(\varphi_g\left(T^{n+1}\right)-\varphi_g\left(T^n\right)\right)\right)\mathbf{I}\right\}^{-1}\\&\quad.\left(\boldsymbol{\varepsilon}^{n+1}-\Lambda\boldsymbol{\varepsilon}_{is}^n-\boldsymbol{\varepsilon}_T^{n+1}\right)\end{aligned} \tag{27}$$

with the consistent tangent matrix $\mathbf{C}$

$$\begin{aligned}\mathbf{C}^{n+1}&=\frac{d\boldsymbol{\sigma}}{d\boldsymbol{\varepsilon}}\\&=\mathbf{C}_r\left[\left(\varphi_g\left(T^{n+1}\right)\mathbf{C}_g^{-1}\mathbf{C}_r\right)+\left(\left(1-\varphi_g\left(T^{n+1}\right)\right)+\kappa_1\Lambda\left(\varphi_g\left(T^{n+1}\right)-\varphi_g\left(T^n\right)\right)\right)\mathbf{I}\right]^{-1}\end{aligned} \tag{28}$$

## 3. Governing equations

In a 2D isotropic fractured medium subjected to a thermomechanical loading (see Fig. 4), the equilibrium and the steady- state heat equations in step n+1 can be written as (indices n+1 are dropped for simplicity):

$$\nabla.\boldsymbol{\sigma}+\mathbf{f}_b=0, \quad \begin{cases}\boldsymbol{\sigma}.\ \mathbf{n}=\mathbf{0} & on\ \ \Gamma_d\\ \boldsymbol{\sigma}.\ \mathbf{n}=\mathbf{t_0} & on\ \ \Gamma_t\\ \mathbf{u}=\mathbf{u_0} & on\ \ \Gamma_u\end{cases} \tag{29}$$

$$\frac{\partial^2T(x,y)}{\partial x^2}+\frac{\partial^2T(x,y)}{\partial y^2}=0, \quad \begin{cases}T=T_0 & on\ \ \Gamma_T\\ q_{normal}=q_0 & on\ \ \Gamma_q\end{cases} \tag{30}$$

where $\boldsymbol{\sigma}=\mathbf{C}\ .\ \boldsymbol{\varepsilon}$ and $\mathbf{C}$ refers to the elasticity tensor introduced in (28). The discretization form of the equilibrium (29) as well as the heat Eq. (30) can be expressed as (Goli et al., 2014):

$$[\mathbf{K}]\{\mathbf{u}\}+\{\mathbf{f}\}=0 \tag{31}$$

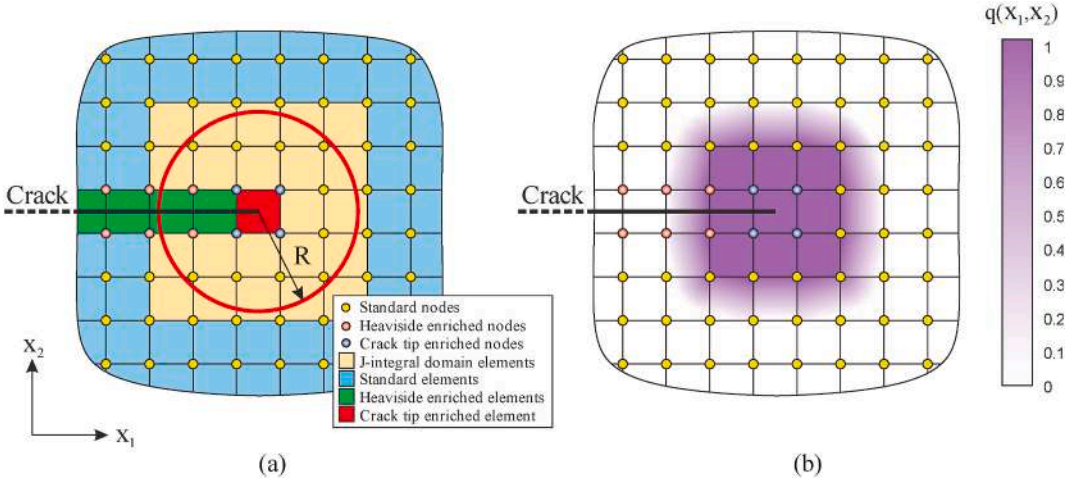


**Fig. 5.** *Equivalent domain integral (a) J domain and (b) Definition of the q function.*

$$\left[\mathbf{K}^{th}\right]\{\mathbf{T}\}+\{\mathbf{f}^{T}\}=0 \tag{32}$$

with

$$\mathbf{f}=\mathbf{f}^{m}+\mathbf{f}^{th}+\mathbf{f}^{is}=\mathbf{f}^{m}+\int_{\Omega}\mathbf{B}^{T}\mathbf{C}\,\boldsymbol{\varepsilon}^{th}d\Omega+\int_{\Omega}\mathbf{B}^{T}\mathbf{C}\,\boldsymbol{\varepsilon}^{is}d\Omega \tag{33}$$

$$\mathbf{K}=\int_{\Omega}\mathbf{B}^{T}\mathbf{C}\mathbf{B}\;d\Omega \tag{34}$$

for the equilibrium equation and

$$\mathbf{f}^{T}=\int_{\Gamma_{th}}\mathbf{N}_{th}^{T}\,q_{th}\;d\Gamma \tag{35}$$

**Table 1**
Thermomechanical update procedure at step n+1.

**a. Known parameters:**
Initial rubber and glass material properties:
$\mathbf{C}_r, \mathbf{C}_g, \alpha_r, \alpha_g$
Variables at loading step n
$T^n, \boldsymbol{\varepsilon}_{is}^n$
Variables at loading step n+1
$T^{n+1}$

**b. Set:**
$\kappa_1, \kappa_2$ according to Eq. (10)
$\varphi_g(T^n), \varphi_g(T^{n+1})$ (Table 2)
$\Lambda$ (Eq. (23))
$\alpha(T^{n+1})$(Table 2)

**c. Compute:**
Consistent tangent matrix $\mathbf{C}(T^n, T^{n+1})$ (Eq. (28))
Thermal force vector $\mathbf{f}^{th}$ (Eq. (33))
Stored force vector $\mathbf{f}^{is}$ (Eq. (33))
Mechanical force vector $\mathbf{f}^m$
Total force vector $\mathbf{f}$ (Eq. (33))
Displacement vector $\mathbf{u}$ (Eq. (31))

**d. Determine:**
Total strain $\boldsymbol{\varepsilon}^{n+1}$ from the displacement vector $\mathbf{u}^{n+1}$
Thermal strain $\boldsymbol{\varepsilon}_T^{n+1} = \alpha(T^{n+1})(T^{n+1} - T^n)$
Mechanical strain $\boldsymbol{\varepsilon}^m = \boldsymbol{\varepsilon}^{n+1} - \Lambda\boldsymbol{\varepsilon}_{is}^n - \boldsymbol{\varepsilon}_T^{n+1}$
Update the stored strain for the next loading step ($\boldsymbol{\varepsilon}_{is}^{n+1}$) using Eq. (23)

**e. Post-processing for fracture parameters:**
Crack opening displacement (COD)
M_integral (Eq. (47))
Stress intensity factors (Eq. (48))

$$\mathbf{K}^{th}=\int_{\Omega}\mathbf{B}_{th}^{T}\mathbf{C}^{th}\mathbf{B}_{th}\;d\Omega \tag{36}$$

for the heat equation. $\mathbf{f}$ is the total force vector, which is composed of the mechanical $\mathbf{f}^m$, the inelastic stored force $\mathbf{f}^{is}$ and the equivalent thermal force $\mathbf{f}^{th}$, $q_{th}$ is the heat flow, $\mathbf{N}$ and $\mathbf{N}_{th}$ are the set of matrices of shape functions including the standard and enrichment functions associated with the displacement and temperature fields, respectively, while $\mathbf{B}$ and $\mathbf{B}_{th}$ refer to their corresponding spatial derivatives. $\mathbf{C}^{th}$ is the diagonal matrix defined as (Hosseini et al., 2013)

$$\mathbf{C}^{th}=\begin{bmatrix}k^{th} & 0\\ 0 & k^{th}\end{bmatrix} \tag{37}$$

where $k^{th}$ is the coefficient of heat conduction as a function of temperature.

## 4. Extended finite element method (XFEM)

Among several methods that exist for modeling fracture problems (like virtual crack closure technique, …), XFEM is probably the most commonly used technique for simulation of general discontinuities. In solving a thermomechanical crack problem using XFEM, the displacement field may be expressed as (Moës et al., 1999; Dolbow and Gosz, 2002; Mohammadi, 2012):

$$\begin{aligned}\mathbf{u}(x)&=\mathbf{u}_{FEM}(x)+\mathbf{u}_{Heaviside}(x)+\mathbf{u}_{tip}(x)\\ &=\sum_{i\in n}N_i(x)\bar{\mathbf{u}}_i+\sum_{j\in n_{Hev}}N_j(x)\left(H(x)-H\left(x_j\right)\right)\bar{\mathbf{p}}_j+\sum_{k\in n_{tip}}N_k(x)\sum_{\alpha=1}^{4}\left(F_\alpha(x)-F_\alpha(x_k)\right)\bar{\mathbf{q}}_k\end{aligned} \tag{38}$$

**Table 2**
SMP material parameters (Volk et al., 2010b).

| Material parameters | Values | Units |
|---|---|---|
| $\alpha_r,\ \alpha_g$ | $5.9\times10^{-4}, 7.0\times10^{-5}$ | $^oC^{-1}$ |
| $E_r,\ E_g$ | 0.39, 1100 | MPa |
| $\nu_r,\ \nu_g$ | 0.48, 0.35 | --- |
| $T_l,\ T_g,\ T_h$ | 25, 72, 90 | $^oC$ |
| $\alpha(T)$ | $\begin{cases}\alpha_r & T\geq T_g\\ \alpha_g & T<T_g\end{cases}$ | $^oC^{-1}$ |
| $\varphi_g(T)$ | $\frac{\tanh((T_h-A)/B)-\tanh((T-A)/B)}{\tanh((T_h-A)/B)-\tanh((T_l-A)/B)}$, $A=345.65$, $B=7.33$ | --- |

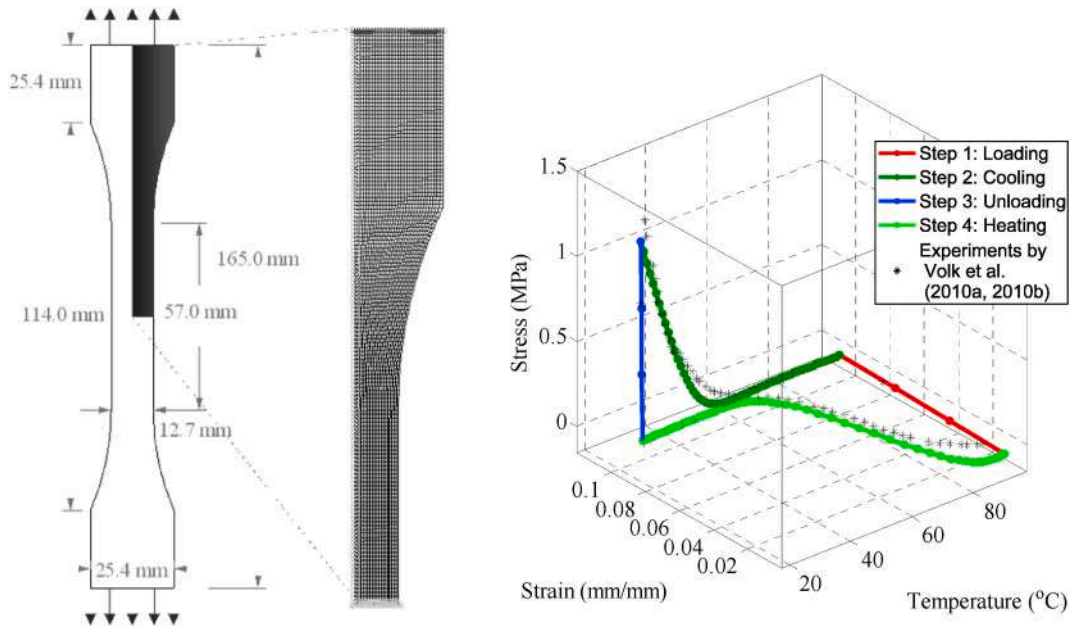


**Fig. 6.** (*a*) *Dimensions of the specimen and mesh, (b) Comparison of the proposed model with the experimental data reported by Volk* et al. (Volk et al., 2010a, 2010b).

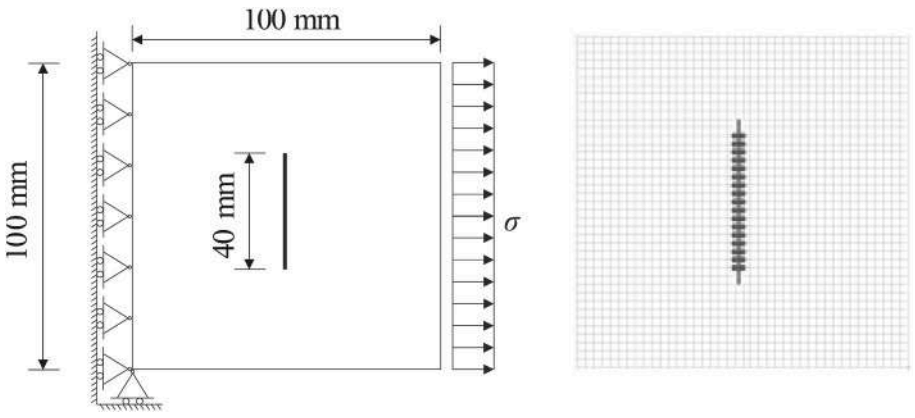


**Fig. 7.** Thermomechanical loading, Geometry, initial boundary conditions and the FE mesh of Example I.

where $\mathbf{u}_{FEM}$, $\mathbf{u}_{Hev}$ and $\mathbf{u}_{tip}$ are, respectively, the standard finite element displacement field, the enriched displacement field corresponding to the Heaviside discontinuity enrichment function and the crack tip enriched part of the displacement. Moreover, $n_{FEM}$ is the set of nodal points of element, $n_{Hev}$ denotes the set of nodes whose elements are bisected by the crack line and $n_{tip}$ is associated with the set of nodes associated with an element which contains a crack tip. Finally, $\overline{\mathbf{u}}_i, \overline{\mathbf{p}}_j, \overline{\mathbf{q}}_k$ are the standard, Heaviside enrichment and the crack tip enriched nodal DOFs, respectively. Moreover, similar to the displacement field, the temperature field can be decomposed as (Goli et al., 2014; Khoei, 2014):

$$\begin{aligned}\mathbf{T}(x) &= \mathbf{T}_{FEM}(x)+\mathbf{T}_{Heaviside}(x)+\mathbf{T}_{tip}(x)\\ &= \sum_{i\in n} N_i(x)\overline{\mathbf{T}}_i + \sum_{j\in n_{Hev}} N_j(x)\big(H(x)-H(x_j)\big)\overline{\mathbf{p}}_j^{th} + \sum_{k\in n_{tip}} N_k(x)\sum_{\alpha=1}^{4}\big(F_\alpha(x)-F_\alpha(x_k)\big)\overline{\mathbf{q}}_k^{th}\end{aligned} \tag{39}$$

where $\overline{\mathbf{T}}$, $\overline{\mathbf{p}}_j^{th}$ and $\overline{\mathbf{q}}_k^{th}$ are the standard and enriched temperature DOFs.

The mechanical as well as the thermal crack tip enrichment functions, obtained from the analytical solutions, have the following forms (Moës et al., 1999; Belytschko and Black, 1999; Zamani et al., 2010):

$$\mathbf{F}^M = \left\{\sqrt{r}\sin\frac{\theta}{2}, \sqrt{r}\cos\frac{\theta}{2}, \sqrt{r}\sin\frac{\theta}{2}\sin\theta, \sqrt{r}\cos\frac{\theta}{2}\sin\theta\right\} \tag{40}$$

$$\mathbf{F}^T = \left\{\sqrt{r}\sin\frac{\theta}{2}\right\} \tag{41}$$

and the definition of the Heaviside function $H(\boldsymbol{x})$ is given by:

$$H(x) = \begin{cases} +1 & \eta(x) \geq 0 \\ -1 & \eta(x) < 0 \end{cases} \tag{42}$$

where (see Fig. 4)

$$\eta(\boldsymbol{x}) = \min\|\boldsymbol{x}-\boldsymbol{x}^d\| sign\big((\boldsymbol{x}-\boldsymbol{x}^d).\ \mathbf{n}_{\Gamma_d}\big) \tag{43}$$

### 4.1. Calculation of SIFs

In order to calculate the SIFs, the well-known J-integral approach is adopted (Rice, 1964):

$$J = \int_\Gamma \left(w\ \delta_{1j} - \sigma_{ij}u_{i,1}\right) n_j\, d\Gamma \tag{44}$$

where $w = \frac{1}{2}\varepsilon_{ij}^{m} C_{ijkl}(T(x))\varepsilon_{kl}^{m}$ is the strain energy density. Taking into account the relation $\varepsilon_{ij}^{m} = \varepsilon_{ij} - \varepsilon_{ij}^{T} - \Lambda\varepsilon_{ij}^{is}$ with $\varepsilon_{ij}^{T} = \alpha_{ij}^{T}(T)\Delta T(x_i)$, the equivalent domain integral (EDI) can be expressed as (Goli et al., 2014; Nikishkov and Atluri, 1987):

$$J = \int_A \left(\sigma_{ij}u_{i,1} - \left(\tfrac{1}{2}\sigma_{ij}\left(\varepsilon_{ij} - \Lambda\varepsilon_{ij}^{is} - \alpha_{ij}^{T}(T(x_i))\Delta T(x_i)\right)\right)\delta_{1j}\right) q_{,j}\, dA + \int_A \left(\sigma_{ij}u_{i,1} - \left(\frac{1}{2}\sigma_{ij}\left(\varepsilon_{ij} - \Lambda\varepsilon_{ij}^{is} - \alpha_{ij}^{T}(T(x_i))\Delta T(x_i)\right)\right)\delta_{1j}\right)_{,j} q dA \tag{45}$$

where $q$ is an arbitrary continuous function taking values between zero at the outer contour and one at the crack tip (Fig. 5).

In addition, summation of the actual ($J_{act}$) and auxiliary ($J_{aux}$) fields yield to the following general form of SIF (Wang et al., 1980)

$$J_{act+aux} = J_{act} + J_{aux} + M \tag{46}$$

where the so-called M-integral is defined as (Goli et al., 2014; Guo et al., 2015):

$$M = \int_A \left[\sigma_{ij}^{Act}u_{i,1}^{Aux} + \sigma_{ij}^{Aux}u_{i,1}^{Act} - \sigma_{ik}^{Aux}\varepsilon_{ik}^{Act\_m}\delta_{1j}\right] q_{,j}\, dA + \int_A \left[\sigma_{ij}^{Act}\left[\left(S_{ijmn}\right)_{tip} - S_{ijmn}\right]\sigma_{mn,1}^{Aux} + \sigma_{ij}^{Aux}\varepsilon_{ij,1}^{Act\_Th}\right] q \quad dA \tag{47}$$

and the SIFs can be calculated using

$$M = \frac{2}{\overline{E}}\left(K_I K_I^{aux} + K_{II}K_{II}^{aux}\right) \tag{48}$$

where

$$\overline{E} = \begin{cases} E & plane\ stress \\ \dfrac{E}{(1-\nu^2)} & plane\ strain \end{cases} \tag{49}$$

Table 1 presents a summary of the computing process, which can be

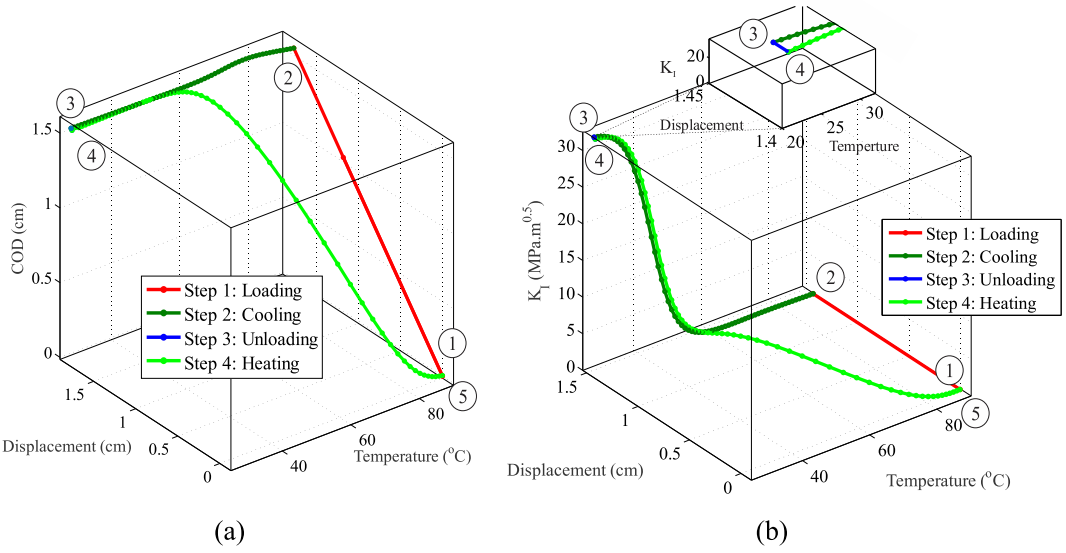


**Fig. 8.** Model prediction of the shape memory effect: stress free- strain recovery. (a) COD-Displacement Temperature profile, (b) $K_I$-Displacement-Temperature profile.

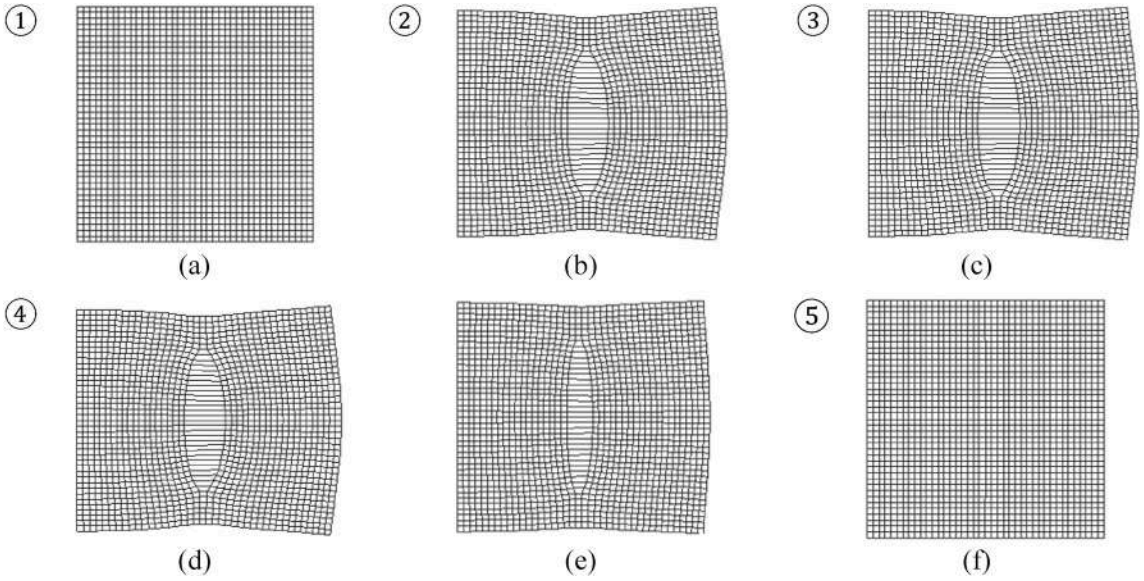


**Fig. 9.** Deformation of the cracked SMP during stress free- strain recovery process in (a) State ①, (b) State ②, (c) State ③, (d) State ④, (e) State between ④ & ⑤, and (f) State ⑤

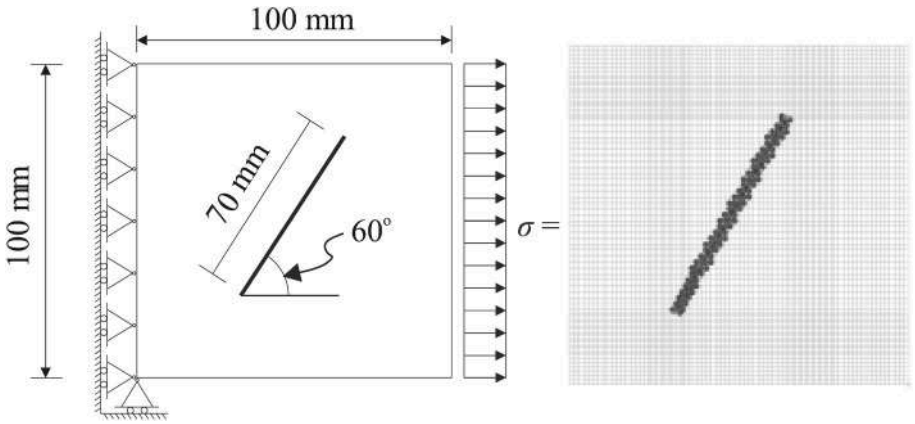


**Fig. 10.** Thermomechanical loading, Geometry, initial boundary conditions and FE mesh of Example II.

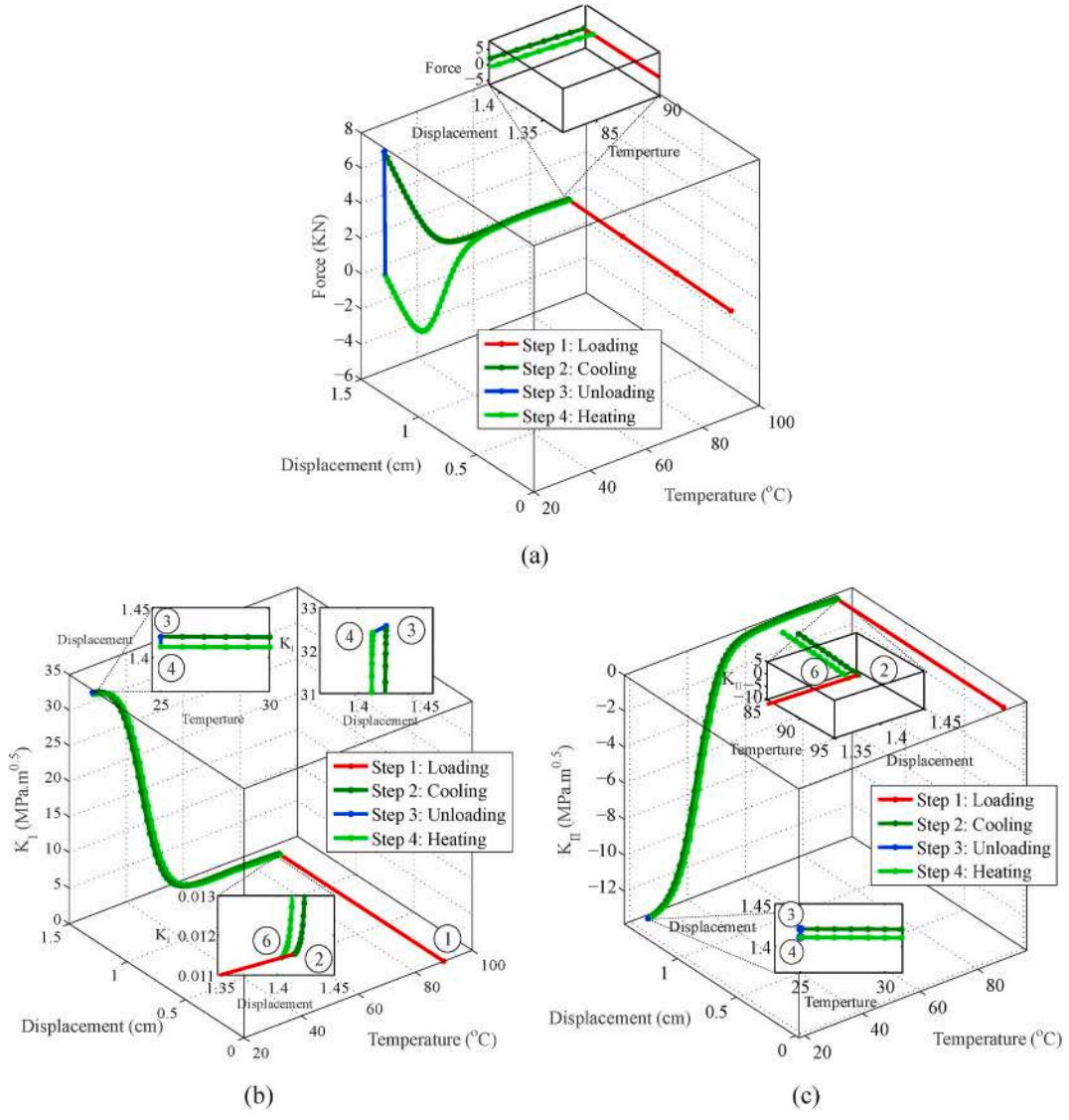


**Fig. 11.** Model prediction of the shape memory effect: stress free- strain recovery. (a) Force-Displacement-Temperature profile, (b) $K_I$ -Displacement-Temperature profile, (b) $K_{II}$-Displacement-Temperature profile.

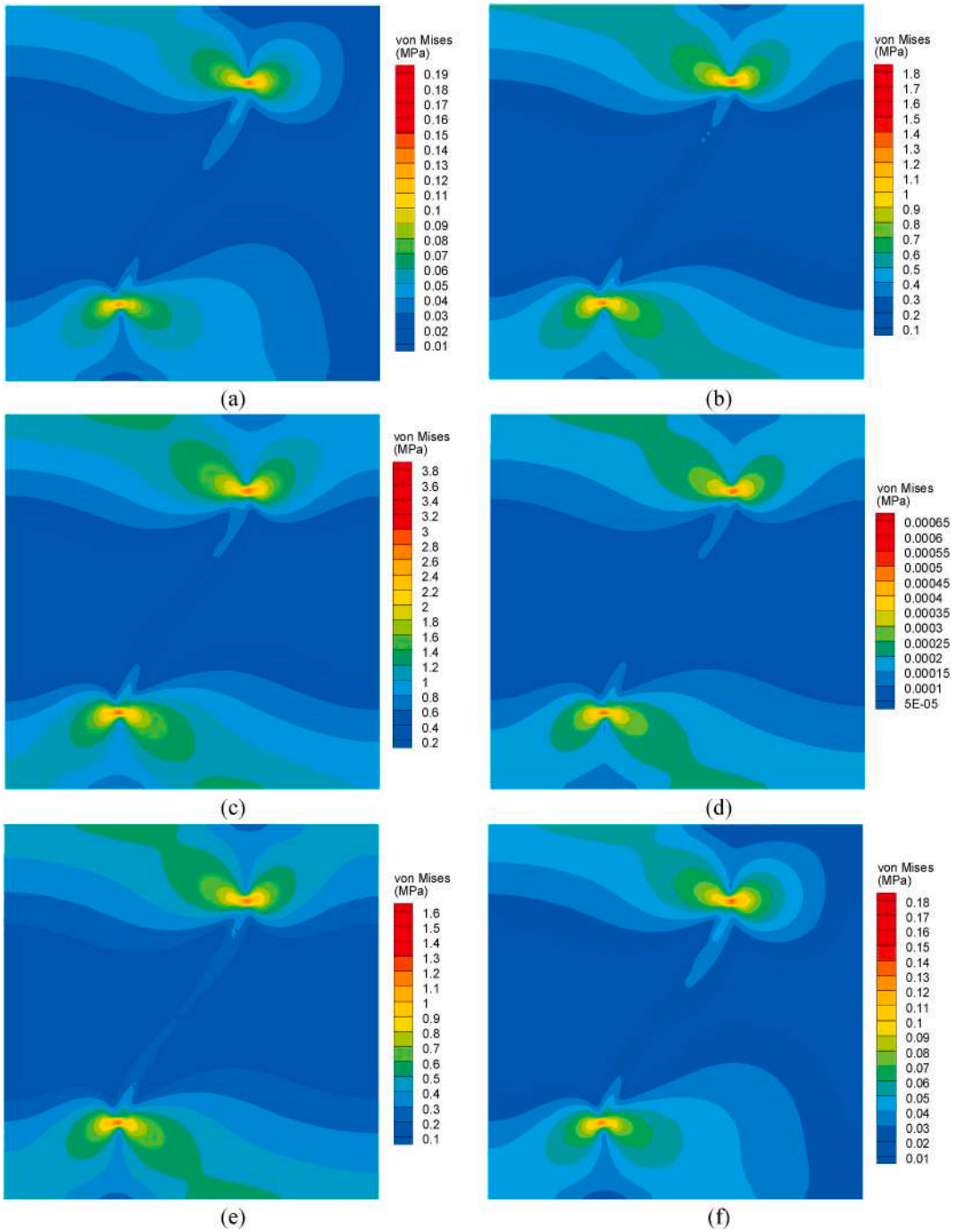


**Fig. 12.** von Mises stress contours for prediction of the shape memory effect: fixed strain-stress recovery (a) State ①, (b) State ②, (c) State ③, (d) State ④, (e) State between ④ & ⑥, and (f) State ⑥. The stress contours in State ① and State ⑥ are similar.

applied to both cooling and heating phases.

## 5. Numerical results

In this section, the proposed constitutive model along with the XFEM approach, is used to investigate the behavior of cracked SMP and to evaluate the fracture parameters in various thermomechanical loading processes. It should be noted that very limited experimental and numerical investigations are available for fracture behavior of SMP materials in comparison with intact SMP samples. The material used in this study is a Veriflex™ with the corresponding material parameters shown in Table 2. Noting the significant characteristics of SMP materials, i.e. the shape memory effect and its sensitivity to temperature, the first and second examples examine this feature in the *Stress free- strain recovery* and the *fixed-strain stress recovery* processes, respectively, for an initially Center Cracked Tension (CCT) specimen. This property is also studied in the third example by examining the behavior of a CCT specimen in which the cracking occurs along the loading path.

The results of the proposed model for a sample under a uniaxial loading, as shown in Fig. 6a are compared with those from the experiments performed by Volk et al., 2010a, 2010b. Fig. 6b clearly shows a reasonable numerical prediction for the experimental results. It should be noted that based on the full recovery assumption for deformations in the idealistic model, the predicted deformation history will conclude in the permanent/recovered shape at the final step, whereas the experimental data exhibit a rather slight shift from the fully-recovered state.

Furthermore, in all examples the energy release rate criterion $G(T) < G_c(T)$ (Malakooti et al., 2014) is satisfied in order to limit the energy release rate $G$, as a function of temperature (Malakooti and Sodano, 2014), to its critical value. $G_c$

**Example I.** Stress free- strain recovery mechanism for an initially cracked SMP

A CCT specimen, shown in Fig. 7, is subjected to a Stress free- strain recovery thermomechanical process. To perform the analysis, 2,800 nodes and 1,600 elements are employed and a plane stress condition is assumed.

Variations of the crack opening displacement (COD) and the mode I stress intensity factor (SIF) during the thermomechanical process of SMP are shown in Figures (8-a) and (8-b), respectively. The obtained thermomechanical cycle, which describes the shape memory effect of the considered SMP, is scrutinized as:

(1) **Loading step** (path ②-①): Starting from state 1, as the rubbery SMP advances towards the state ②, the crack opens under a purely mechanical loading (Fig. 8-a), leading to an increase in the stress intensity factor (Fig. 8-b).
(2) **Cooling step** (path -②③): In this step, by decreasing the ambient temperature, while keeping the two ends of the plate fixed, it is observed that the crack opening displacement remains unchanged (Fig. 8-a). Moreover, due to the increase in the elasticity modulus of material, the stress intensity factor increases significantly (Fig. 8-b).
(3) **Unloading step** (path ③-④): After unloading the specimen, the glassy SMP still stays in its temporary shape due to the presence of inelastic stored strains at the state ④. As a result, a slight decrease is observed in the crack opening displacement (Fig. 8-a) as well as the stress intensity factor (Fig. 8-b) (about 0.4%).
(4) **Heating step** (path ④-⑤): Finally, by heating the specimen and making the SMP to gradually transform from the glassy to the rubbery phase, the material recovers its permanent shape, and the crack starts to close (Fig. 8-a), with a vanishing stress intensity factor (state ⑤ in Fig. 8-b). Moreover, deformation of the cracked specimen during this thermomechanical process is shown in Fig. 9.

**Example II.** Fixed strain- stress recovery mechanism for an initially cracked SMP

In this example, an inclined cracked specimen with the dimensions shown in Fig. 10 is placed under a Fixed strain- stress recovery thermomechanical process. The analysis is performed in plane stress condition using 2,800 nodes and 1,600 elements.

The resulting thermomechanical cycle is shown in Fig. 11-a, where, as expected, the response to the loading conditions are similar to the previous example for the first three steps. Fig. 11-b and Fig. 11-c show the variations of mode I and II SIFs during the fixed strain- stress recovery cycle, respectively. In the first loading step, the rubbery SMP is associated with an increase in the stress intensity factors under pure mechanical loading. In the cooling process, and by decreasing the

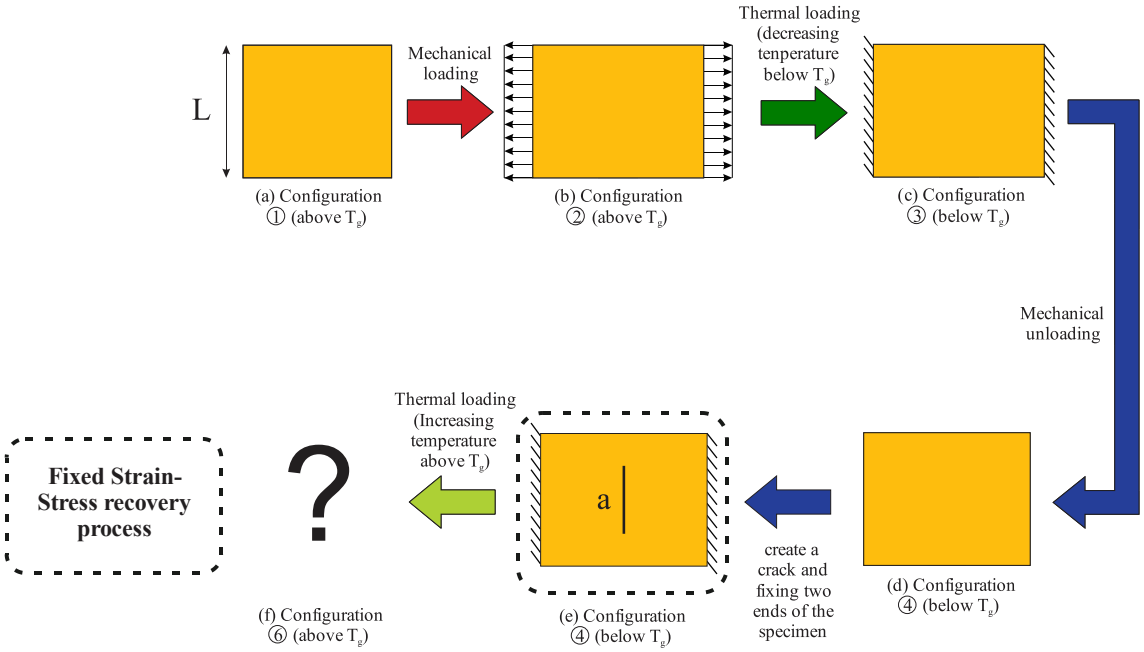


**Fig. 13.** Thermomechanical loading cycle of Example III. The sample is cracked at state ④

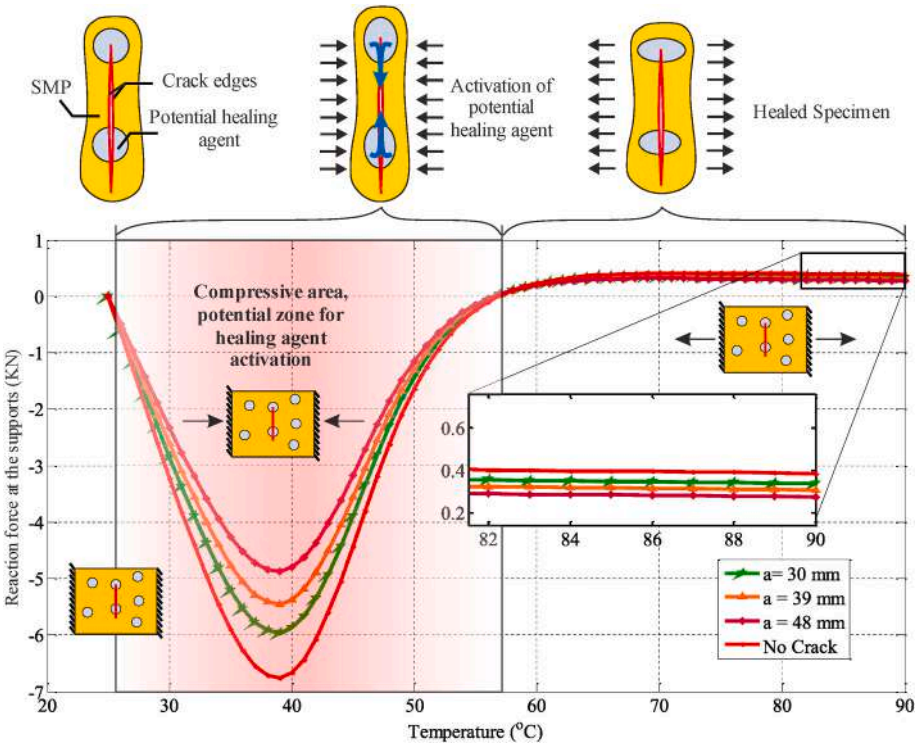


**Fig. 14.** Variation of the reaction forces in the recovery process with temperature for different crack lengths.

temperature, as the SMP transforms from the rubbery phase to the glassy phase, the stresses, and the stress intensity factors, increase significantly, as illustrated in Fig. 11-b, c. In the next step, by unloading the sample, the mechanical stresses vanish while the stress intensity factors slightly reduce due to the presence of stored strains.

In the final step, (i.e. path ④-⑤), by increasing the temperature while keeping the two ends of the plate fixed, as Fig. 11-a demonstrates, the configuration associated with state ② is recovered reasonably well at the end of the thermomechanical process at state ⑤. This outcome can also be further examined by comparing the values of stress intensity factors (Fig. 11-b,c) as well as the stress contours (Fig. 12) at states ② and ⑤. It is noteworthy to mention that at the initial steps of the recovery process, despite the presence of compressive reactions at the two ends of the sample, which correspond to compressive mechanical stresses in the specimen, the crack closure is impeded due to the presence of stored strains. Hence, the stress intensity factors admit nonzero values during the heating process.

Moreover, the SIFs decrease throughout this process due to the reduction of the modulus of elasticity, i.e., the reduction of internal stresses.

**Example III**. Fixed strain- stress recovery mechanism of an SMP plate cracked at the unloading state

In many applications of SMPs, such as in surgical vascular stents, the manufacturing process usually proceeds up to state (4) of the thermomechanical cycle. The heating process, however, which is actually needed for recovery and healing purposes, is exercised when the SMP is at service. It has also been realized that, at state (4), the SMP material is prone to cracking owing to inappropriate storage, poor transportation conditions, etc (Nji and Li, 2012; Li and Uppu, 2010). As a result, investigation of the cracking of SMPs and examination of such defects on the SME property can be beneficial for their optimal design. For this purpose, an intact plate under thermomechanical loading cycle (①-②-③-④) is considered, as shown in Fig. 13 with the dimensions as well as thermomechanical loading values similar to Fig. 7. Thereafter, by assuming a sudden (mode I) crack of length "a" at state ④, the changes in its force recovery are investigated in the heating process, as presented in Fig. 13.

The results, illustrated in Fig. 14, show that by increasing the crack length, the reaction force at the supports along the path ④-⑥ is expectedly reduced due to decreasing material stiffness. Moreover, Fig. 14 shows that by decreasing the crack length, the final reactions would be closer to the no cracked condition. Clearly, it can be concluded that the reaction force necessary to activate a potential healing agent (specially at temperatures below 57 °C) decreases by increasing the crack length, which means that the healing potential decreases by increasing the crack size. If the ratio of the reaction force calculated at state ⑥ for crack length "a" to the force applied in the initial step of the uncracked plate, that is state ②, is defined as the recovery force ratio,

$$Recovery\ \ force\ \ ratio\ \ (\%) = \frac{Reaction\ \ force\ \ at\ \ state\ \ ⑥}{Applied\ \ force\ \ at\ \ state\ \ ②} \times 100 \tag{50}$$

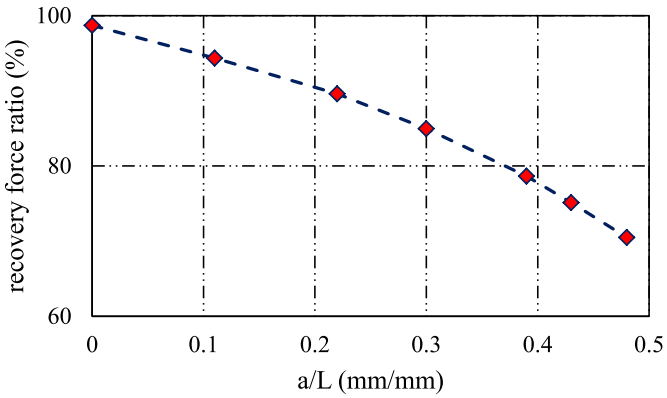


**Fig. 15.** Variation of recovery force ratio (%) with a/L.

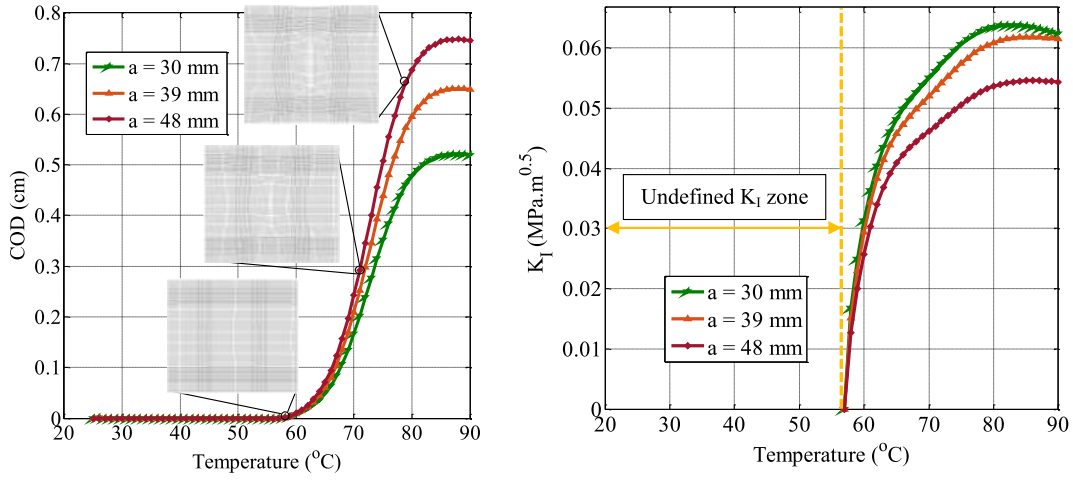


(a) (b)

**Fig. 16.** (a) Variation of the crack opening displacement (COD) with temperature, (b) Variation of the mode I stress intensity factor ($K_I$) with temperature.

Variations of this parameter versus the normalized crack length ($a/L$, L is the plate width at initial configuration, see Fig. 13a) are shown in Fig. 15, which shows the higher rate of change in the recovery force ratio as the crack length increases.

Moreover, variation of the crack opening displacement (COD) with temperature is shown in Fig. 16-a. In the early stages of rising temperature (up to 57 °C), compressive stresses occur in the plate due to the prevalence of thermal strains over the released inelastic stored strains, resulting in closing the two crack faces and vanishing COD. Both the Lagrange and Penalty methods may be used to impose the impenetrability condition of crack faces.

By increasing the temperature beyond 57 °C, the release of inelastic stored strains gradually becomes dominant, enforcing the original shape of the sample to recover. Therefore, the stresses in the plate become tensile and the crack gradually opens, leading to an increase of the stress intensity factor. Fig. 16-a,b demonstrate these phenomena in more detail. It is important to mention that the stress intensity factor cannot be defined below the 57 °C, due to compressive total stresses (Fig. 16-b).

## 6. Conclusion

The main purpose of this study has been to investigate the fracture behavior of shape memory polymers and to examine their healing potentials under various thermomechanical loadings. Employing a phase transition based SMP constitutive model and applying XFEM for crack modeling, the fracture behavior of SMPs in two conventional thermomechanical cycles, namely the *fixed strain- stress recovery* and *stress free- strain recovery*, has been investigated. In both thermomechanical cycles, it is observed that by unloading the sample at the end of third loading step, the mechanical stresses vanish while the stress intensity factors, as well as COD value, slightly reduce due to the presence of inelastic stored strains.

Moreover, it is observed that if a crack is created on an SMP plate in the initial state of the *stress free- strain recovery* cycle, the crack is completely closed at the end of such thermomechanical process. It is worth mentioning that during the recovery process, it is a common practice to use additive nanoparticles (such as microcapsules, microfibers, etc.) as the healing agents in order to heal the defect once the crack edges meet (state ⑤ from Fig. 8-a). This very process is known as the "Close Then Heal (CTH)" technique, which can be applied in healing polymers. Therefore, the first step of the SMP healing process, namely closing crack, is accomplished and the healing step can be further carried out by other means such as polymer additives.

Furthermore, at the end of the *fixed strain- stress recovery* cycle, it is observed that the plate has almost recovered the stresses created in the first step of the thermomechanical loading and the shape memory property has been successfully resembled. It is also observed that the stress intensity factors along with the crack opening displacements are fully recovered in such thermomechanical cycle.

In addition, by creating a crack on the shape-memory polymer in the midst of the thermomechanical process in the *fixed strain- stress recovery* cycle, it is observed that the value of the reaction force in the recovery process has been reduced as the crack length increases. In other words, the performance of the structure in providing the desired reaction forces in the recovery process has been reduced. In addition, the crack opening displacement at the end of this cycle increases by increasing the crack length. However, the stress intensity factor decreases by increasing the crack length due to the dramatic decrease in stresses. In this example, in addition to crack closure, the presence of compressive forces in the initial steps of force recovery cycle may clearly contribute to heal the crack if microcapsule healing agents are employed. Therefore, one may design an SMP composite where the type as well as the amount of the additive(s) required in the SMP matrix can be designed to allow for the defects to heal and the composite to work efficiently. Further development of the methodology to large deformation conditions is the subject of an independent study.

## Credit statement

**Alireza Foyouzat**: Conceptualization, Methodology, Software, Writing- Original draft preparation, Validation. **Hamid Bayesteh**: Review, Discussion. **Soheil Mohammadi**: Supervision, Writing- Reviewing and Editing.

## Declaration of competing interest

The authors declare that they have no known competing financial interests or personal relationships that could have appeared to influence the work reported in this paper.

## References


Abbasi-Shirsavar, M., Baghani, M., Taghavimehr, M., Golzar, M., Nikzad, M., Ansari, M., George, D., 2019. An experimental–numerical study on shape memory behavior of PU/PCL/ZnO ternary blend. J. Intell. Mater. Syst. Struct. 30, 116–126. https://doi.org/10.1177/1045389X18803459.

Baghani, M., Naghdabadi, R., Arghavani, J., Sohrabpour, S., 2012a. A constitutive model for shape memory polymers with application to torsion of prismatic bars. J. Intell. Mater. Syst. Struct. 23, 107–116. https://doi.org/10.1177/1045389X11431745.

Baghani, M., Naghdabadi, R., Arghavani, J., Sohrabpour, S., 2012b. A thermodynamically-consistent 3 D constitutive model for shape memory polymers. Int. J. Plast. 35, 13–30. https://doi.org/10.1016/j.ijplas.2012.01.007.

Baniasadi, M., Foyouzat, A., Baghani, M., 2020. Multiple shape memory effect for smart helical springs with variable stiffness over time and temperature. Int. J. Mech. Sci. 182, 105742. https://doi.org/10.1016/j.ijmecsci.2020.105742.

D.L.-I.J. Of, U. Baxevanis, T., Parrinello, A.F., Lagoudas, D.C., 2013. On the fracture toughness enhancement due to stress-induced phase transformation in shape memory alloys Int. J. Plast. 50, 158–169. https://doi.org/10.1016/j.ijplas.2013.04.007.

Belytschko, T., Black, T., 1999. Elastic crack growth in finite elements with minimal remeshing. Int. J. Numer. Methods Eng. 45, 601–620. https://doi.org/10.1002/(SICI)1097-0207(19990620)45:5<601::AID-NME598>3.0. CO;2-S.

Boatti, E., Scalet, G., Auricchio, F., 2016. A three-dimensional finite-strain phenomenological model for shape-memory polymers: formulation, numerical simulations, and comparison with experimental data. Int. J. Plast. 83, 153–177. https://doi.org/10.1016/j.ijplas.2016.04.008.

Chen, Y.C., Lagoudas, D.C., 2008a. A constitutive theory for shape memory polymers. Part I. Large deformations. J. Mech. Phys. Solid. 56, 1752–1765. https://doi.org/10.1016/j.jmps.2007.12.005.

Chen, Y.C., Lagoudas, D.C., 2008b. A constitutive theory for shape memory polymers. Part II. A linearized model for small deformations. J. Mech. Phys. Solid. 56, 1766–1778. https://doi.org/10.1016/j.jmps.2007.12.004.

Chen, T., Bilal, O.R., Lang, R., Daraio, C., Shea, K., 2019. Autonomous deployment of a solar panel using elastic origami and distributed shape-memory-polymer actuators. Physical Review Applied 11, 64069. https://doi.org/10.1103/PhysRevApplied.11.064069.

Diani, J., Liu, Y., Gall, K., 2006. Finite strain 3D thermoviscoelastic constitutive model for shape memory polymers. Polym. Eng. Sci. 46, 486–492. https://doi.org/10.1002/pen.20497.

Diani, J., Frédy, C., Gilormini, P., Merckel, Y., Régnier, G., Rousseau, I., 2011. A torsion test for the study of the large deformation recovery of shape memory polymers. Polym. Test. 30, 335–341. https://doi.org/10.1016/j.polymertesting.2011.01.008.

Diani, J., Gilormini, P., Frédy, C., Rousseau, I., 2012. Predicting thermal shape memory of crosslinked polymer networks from linear viscoelasticity. Int. J. Solid Struct. 49, 793–799. https://doi.org/10.1016/j.ijsolstr.2011.11.019.

Dolbow, J.E., Gosz, M., 2002. On the computation of mixed mode stress intensity factors in functionally graded materials. Int. J. Solid Struct. 39, 2557–2574. https://doi.org/10.1016/S0020-7683(02)00114-2.

Du, Z., Zeng, X.M., Liu, Q., Lai, A., Amini, S., Miserez, A., Schuh, C.A., Gan, C.L., 2015. Size effects and shape memory properties in ZrO2 ceramic micro- and nano-pillars. Scripta Mater. 101, 40–43. https://doi.org/10.1016/j.scriptamat.2015.01.013.

Fatemi Dehaghani, P., Hatefi Ardakani, S., Bayesteh, H., Mohammadi, S., 2017. 3D hierarchical multiscale analysis of heterogeneous SMA based materials. Int. J. Solid Struct. 118–119, 24–40. https://doi.org/10.1016/j.ijsolstr.2017.04.025.

Foyouzat, A., Bayesteh, H., Mohammadi, S., 2020. A brittle to ductile phase transition fracture analysis of shape memory polymers. Eng. Fract. Mech. 224, 106751. https://doi.org/10.1016/j.engfracmech.2019.106751.

Goli, E., Bayesteh, H., Mohammadi, S., 2014. Mixed mode fracture analysis of adiabatic cracks in homogeneous and non-homogeneous materials in the framework of partition of unity and the path-independent interaction integral. Eng. Fract. Mech. 131, 100–127. https://doi.org/10.1016/j.engfracmech.2014.07.013.

Govindarajan, T., Shandas, R., 2014. A survey of surface modification techniques for next-generation shape memory polymer stent devices. Polymers 6, 2309–2331. https://doi.org/10.3390/polym6092309.

Gu, J., Leng, J., Sun, H., Zeng, H., Cai, Z., 2019. Thermomechanical constitutive modeling of fiber reinforced shape memory polymer composites based on thermodynamics with internal state variables. Mech. Mater. 130, 9–19. https://doi.org/10.1016/j.mechmat.2019.01.004.

Guo, F., Huang, K., Guo, L., Bai, X., Zhong, S., Yu, H., 2015. An interaction energy integral method for T-stress evaluation in nonhomogeneous materials under thermal loading. Mech. Mater. 83, 30–39. https://doi.org/10.1016/j.mechmat.2014.11.007.

Han, X.J., Dong, Z.Q., Fan, M.M., Liu, Y., Li, J.H., Wang, Y.F., Yuan, Q.J., Li, B.J., Zhang, S., 2012. PH-induced shape-memory polymers. Macromol. Rapid Commun. 33, 1055–1060. https://doi.org/10.1002/marc.201200153.

Hatefi Ardakani, S., Afshar, A., Mohammadi, S., 2016. Numerical study of thermo-mechanical coupling effects on crack tip fields of mixed-mode fracture in pseudoelastic shape memory alloys. Int. J. Solid Struct. 81, 160–178. https://doi.org/10.1016/j.ijsolstr.2015.11.023.

Hatefi Ardakani, S., Moslemzadeh, H., Mohammadi, S., 2019. Delamination analysis in bimaterials consisting of shape memory alloy and elastoplastic layers. Compos. Struct. 225. https://doi.org/10.1016/j.compstruct.2019.111149.

Hosseini, S.S., Bayesteh, H., Mohammadi, S., 2013. Thermo-mechanical XFEM crack propagation analysis of functionally graded materials. Mater. Sci. Eng. 561, 285–302. https://doi.org/10.1016/j.msea.2012.10.043.

Karimi, M., Bayesteh, H., Mohammadi, S., 2019. An adapting cohesive approach for crack-healing analysis in SMA fiber-reinforced composites. Comput. Methods Appl. Mech. Eng. 349, 550–575. https://doi.org/10.1016/j.cma.2019.02.019.

Kazemi-Lari, M.A., Malakooti, M.H., Sodano, H.A., 2017. Active photo-thermal self-healing of shape memory polyurethanes. Smart Mater. Struct. 26. https://doi.org/10.1088/1361-665X/aa677d.

Khoei, A.R., 2014. Extended Finite Element Method: Theory and Applications.

Lendlein, A., Jiang, H., Jünger, O., Langer, R., 2005. Light-induced shape-memory polymers. Nature 434, 879–882. https://doi.org/10.1038/nature03496.

Leng, Jinsong, Lu, Haibao, Liu, Yanju, Huang, Wei Min, Du, Shanyi, 2009. Shape-Memory Polymers—A Class of Novel Smart Materials. http://www.paper.edu.cn.

Leng, J., Lan, X., Liu, Y., Du, S., 2011. Shape-memory polymers and their composites: stimulus methods and applications. Prog. Mater. Sci. 56, 1077–1135. https://doi.org/10.1016/j.pmatsci.2011.03.001.

Leo, S.Y., Zhang, W., Zhang, Y., Ni, Y., Jiang, H., Jones, C., Jiang, P., Basile, V., Taylor, C., 2018. Chromogenic photonic crystal sensors enabled by multistimuli-responsive shape memory polymers. Small 14. https://doi.org/10.1002/smll.201703515.

Li, G., Uppu, N., 2010. Shape memory polymer based self-healing syntactic foam: 3-D confined thermomechanical characterization. Compos. Sci. Technol. 70, 1419–1427. https://doi.org/10.1016/j.compscitech.2010.04.026.

Liu, Y., Gall, K., Dunn, M.L., McCluskey, P., 2004. Thermomechanics of shape memory polymer nanocomposites. Mechanics of Materials, pp. 929–940. https://doi.org/10.1016/j.mechmat.2003.08.012.

Liu, Y., Gall, K., Dunn, M.L., Greenberg, A.R., Diani, J., 2006. Thermomechanics of shape memory polymers: uniaxial experiments and constitutive modeling. Int. J. Plast. 22, 279–313. https://doi.org/10.1016/j.ijplas.2005.03.004.

Liu, Y., Lv, H., Lan, X., Leng, J., Du, S., 2009. Review of electro-active shape-memory polymer composite. Compos. Sci. Technol. 69, 2064–2068. https://doi.org/10.1016/j.compscitech.2008.08.016.

Liu, Y., Du, H., Liu, L., Leng, J., 2014. Shape memory polymers and their composites in aerospace applications: a review. Smart Mater. Struct. 23 https://doi.org/10.1088/0964-1726/23/2/023001.

Malakooti, M.H., Sodano, H.A., 2014. Toughening response of a crack-tip surrounded by a local elastic gradient. Smart Mater. Struct. 23. https://doi.org/10.1088/0964-1726/23/3/035009.

Malakooti, M.H., Anderson, P.L., Sodano, H.A., 2014. Toughening mechanism of heterogeneous aliphatic polyurethanes. Polymer 55, 2086–2093. https://doi.org/10.1016/j.polymer.2014.03.002.

Maletta, C., Bruno, L., Corigliano, P., Crupi, V., Guglielmino, E., 2014. Crack-tip thermal and mechanical hysteresis in shape memory alloys under fatigue loading. Mater. Sci. Eng. 616, 281–287. https://doi.org/10.1016/j.msea.2014.08.007.

Moës, N., Dolbow, J., Belytschko, T., 1999. A finite element method for crack growth without remeshing. Int. J. Numer. Methods Eng. 46, 131–150. https://doi.org/10.1002/(SICI)1097-0207(19990910)46:1<131::AID-NME726>3.0. CO;2-J.

Mohammadi, S., 2012. XFEM Fracture Analysis of Composites. John Wiley & Sons Inc.

Moshkelgosha, E., Mamivand, M., 2020. Phase field modeling of crack propagation in shape memory ceramics – application to zirconia. Comput. Mater. Sci. 174, 109509. https://doi.org/10.1016/j.commatsci.2019.109509.

Nikishkov, G.P., Atluri, S.N., 1987. An equivalent domain integral method for computing crack-tip integral parameters in non-elastic, thermo-mechanical fracture. Eng. Fract. Mech. 26, 851–867. https://doi.org/10.1016/0013-7944(87)90034-8.

Nji, J., Li, G., 2012. Damage healing ability of a shape-memory-polymer-based particulate composite with small thermoplastic contents. Smart Mater. Struct. 21. https://doi.org/10.1088/0964-1726/21/2/025011.

Plaisted, T.A., Nemat-Nasser, S., 2007. Quantitative evaluation of fracture, healing and re-healing of a reversibly cross-linked polymer. Acta Mater. 55, 5684–5696. https://doi.org/10.1016/j.actamat.2007.06.019.

Rice, J.R., 1964. A path independent integral and the approximate analysis of strain concentration by notches and cracks. Journal of Applied Mechanics, Transactions ASME. 35, 379–388. https://doi.org/10.1115/1.3601206.

Tavangarian, F., Li, G., 2015. Crack-healing in spinel (MgAl2O4) ceramic. Mater. Sci. Eng. 641, 201–209. https://doi.org/10.1016/j.msea.2015.06.045.

Tobushi, H., Hashimoto, T., Hayashi, S., Yamada, E., 1997. Thermomechanical constitutive modeling in shape memory polymer of polyurethane series. J. Intell. Mater. Syst. Struct. 8, 711–718. https://doi.org/10.1177/1045389X9700800808.

Volk, B.L., Lagoudas, D.C., Chen, Y.C., Whitley, K.S., 2010a. Analysis of the finite deformation response of shape memory polymers: I. Thermomechanical characterization. Smart Mater. Struct. 19 https://doi.org/10.1088/0964-1726/19/7/075005.

Volk, B.L., Lagoudas, D.C., Chen, Y.C., 2010b. Analysis of the finite deformation response of shape memory polymers: II. 1D calibration and numerical implementation of a finite deformation, thermoelastic model. Smart Mater. Struct. 19 https://doi.org/10.1088/0964-1726/19/7/075006.

Wang, S.S., Yau, J.F., Corten, H.T., 1980. A mixed-mode crack analysis of rectilinear anisotropic solids using conservation laws of elasticity. Int. J. Fract. 16, 247–259. https://doi.org/10.1007/BF00013381.

Wang, G.Z., Xuan, F.Z., Tu, S.T., Wang, Z.D., 2010. Effects of triaxial stress on martensite transformation, stress-strain and failure behavior in front of crack tips in shape memory alloy NiTi. Mater. Sci. Eng. 527, 1529–1536. https://doi.org/10.1016/j.msea.2009.10.038.

Yarali, E., Taheri, A., Baghani, M., 2020. A comprehensive review on thermomechanical constitutive models for shape memory polymers. J. Intell. Mater. Syst. Struct. 31, 1243–1283. https://doi.org/10.1177/1045389X20916795.

Zamani, A., Gracie, R., Eslami, M.R., 2010. Higher order tip enrichment of eXtended Finite Element Method in thermoelasticity. Comput. Mech. 46, 851–866. https://doi.org/10.1007/s00466-010-0520-2.

Zeng, H., Leng, J., Gu, J., Sun, H., 2018. A thermoviscoelastic model incorporated with uncoupled structural and stress relaxation mechanisms for amorphous shape memory polymers. Mech. Mater. 124, 18–25. https://doi.org/10.1016/j.mechmat.2018.05.010.

Zhang, P., Arceneaux, D.J., Liu, Z., Nikaeen, P., Khattab, A., Li, G., 2018. A crack healable syntactic foam reinforced by 3D printed healing-agent based honeycomb. Compos. B Eng. 151, 25–34. https://doi.org/10.1016/j.compositesb.2018.06.005.

Zhao, W., Liu, L., Leng, J., Liu, Y., 2020. Thermo-mechanical behavior prediction of shape memory polymer based on the multiplicative decomposition of the deformation gradient. Mech. Mater. 143, 103263. https://doi.org/10.1016/j.mechmat.2019.103263.